Editors' Suggestion

Room-Temperature Magnetic Phase Transition in an Electrically Tuned van der Waals Ferromagnet

Cheng Tan,[1,4,*] Ji-Hai Liao,[2,*] Guolin Zheng,[3,†] Meri Algarni,[4,5] Jia-Yi Lin,[2] Xiang Ma,[6] Edwin L. H. Mayes,[7] Matthew R. Field,[7] Sultan Albarakati,[4,8] Majid Panahandeh-Fard,[4] Saleh Alzahrani,[4] Guopeng Wang,[9] Yuanjun Yang,[1] Dimitrie Culcer,[10] James Partridge,[4] Mingliang Tian,[3,9] Bin Xiang,[6,‡] Yu-Jun Zhao,[2,§] and Lan Wang[1,4,‖]

[1]*Lab of Low Dimensional Magnetism and Spintronic Devices, School of Physics, Hefei University of Technology, Hefei, Anhui 230009, China*

[2]*Department of Physics, South China University of Technology, Guangzhou 510640, China*

[3]*Anhui Province Key Laboratory of Condensed Matter Physics at Extreme Conditions, High Magnetic Field Laboratory, Chinese Academy of Sciences (CAS), Hefei, Anhui 230031, China*

[4]*ARC Centre of Excellence in Future Low-Energy Electronics Technologies (FLEET), School of Science, RMIT University, Melbourne, Victoria 3001, Australia*

[5]*Physics Department, Faculty of Science, Al-Baha University, Alaqiq 65779, Saudi Arabia*

[6]*Hefei National Laboratory for Physical Sciences at the Microscale, Department of Materials Science & Engineering, CAS Key Lab of Materials for Energy Conversion, University of Science and Technology of China, Hefei, Anhui 230026, China*

[7]*RMIT Microscopy & Microanalysis Facility, RMIT University, Melbourne, Victoria 3000, Australia*

[8]*Physics Department, Faculty of Science and Arts, University of Jeddah, P.O. Box 80200, 21589 Khulais, Saudi Arabia*

[9]*Department of Physics, School of Physics and Materials Science, Anhui University, Hefei, Anhui 230601, China*

[10]*School of Physics and ARC Centre of Excellence in Future Low-Energy Electronics Technologies, UNSW Node, University of New South Wales, Sydney, New South Wales 2052, Australia*

(Received 11 October 2022; revised 10 April 2023; accepted 6 September 2023; published 17 October 2023)

Finding tunable van der Waals (vdW) ferromagnets that operate at above room temperature is an important research focus in physics and materials science. Most vdW magnets are only intrinsically magnetic far below room temperature and magnetism with square-shaped hysteresis at room temperature has yet to be observed. Here, we report magnetism in a quasi-2D magnet $Cr_{1.2}Te_2$ observed at room temperature (290 K). This magnetism was tuned via a protonic gate with an electron doping concentration up to 3.8×10^{21} cm^{-3}. We observed nonmonotonic evolutions in both coercivity and anomalous Hall resistivity. Under increased electron doping, the coercivities and anomalous Hall effects (AHEs) vanished, indicating a doping-induced magnetic phase transition. This occurred up to room temperature. DFT calculations showed the formation of an antiferromagnetic (AFM) phase caused by the intercalation of protons which induced significant electron doping in the $Cr_{1.2}Te_2$. The tunability of the magnetic properties and phase in room temperature magnetic vdW $Cr_{1.2}Te_2$ is a significant step towards practical spintronic devices.

DOI: 10.1103/PhysRevLett.131.166703

Electrical manipulation of magnetic properties is essential for the development of low-energy spintronic devices [1–5]. In recent years, the emergence of van der Waals (vdW) magnets has increased the synergy between spintronics and two-dimensional (2D) materials [6–11]. For the next generation of low-energy vdW spintronic devices, electrically tunable magnetic properties will be vital. To date, various electrically tuned magnetic properties, such as magnetization [12], coercivity [13], magnetic anisotropy [14], magnetic phase transition (MPT) [15,16], and exchange bias [17,18] have been observed in vdW magnets and heterostructures. However, these phenomena have only been observed at low temperatures. Recently, chromium chalcogenides (Cr_aX_b, $X = S$, Se, and Te), a class of layered or quasilayered structure magnets, have exhibited interesting and potentially exploitable magnetic characteristics at higher temperature [19–28]. Among them, Cr_aTe_b materials have exhibited high Curie temperatures and, more importantly, remanence and perpendicular magnetic anisotropy that appear to remain significant (i.e., near square-shaped hysteresis loop exhibited) at room temperature [29]. These materials thus hold promise for future applications and may be suitable platforms for room-temperature studies of electric gate-controlled magnetism. However, Cr_aTe_b materials are metallic and thus difficult to electrically tune using standard dielectric layers. Ionic gating techniques have recently proved successful in elevating the Curie temperature of Fe_3GeTe_2 to room

temperature while the low remanence at room temperature limits its broader application in spintronics [30]. Notably, a solid protonic gating technique [16–18,31] has proved effective in altering the magnetic characteristics of vdW metals.

Here, for the first time, we report an electrically tuned phase transition from ferromagnetism (FM) to antiferromagnetism (AFM) in a vdW magnet with near square-shaped loops at room temperature (290 K), using proton-gated $Cr_{1.2}Te_2$ nanoflakes. In this work, the magnetism of a pristine $Cr_{1.2}Te_2$ nanoflake was first investigated under magnetic fields applied perpendicular to its surface. These experiments revealed square-shaped anomalous Hall effect (AHE) loops which persisted at temperatures exceeding 50 K and indicated the existence of a perpendicular magnetic anisotropy. Solid protonic gates were then added and these were used to modulate the magnetism of $Cr_{1.2}Te_2$ nanoflakes at 200 K. The results of these experiments demonstrated that electron doping concentrations up to 3.8×10^{21} cm^{-3} could be achieved with proton intercalation. The AHE resistivity (ρ_{AHE}) and coercivity were effectively tuned with gate voltage. Finally, the magnetism of a $Cr_{1.2}Te_2$ nanoflake was electrically tuned at 290 K, resulting in coercivity and ρ_{AHE} exhibiting acute evolution that resembled the characteristics measured at 200 K. The AHE loops of all $Cr_{1.2}Te_2$ nanoflake devices vanished under high gate voltages. This behavior is attributed to MPT. Supporting DFT calculations indicate that a transition from FM to AFM occurs due to proton-intercalation-induced electron doping within the $Cr_{1.2}Te_2$. The calculated anomalous Hall conductivity (AHC) varied significantly near the Fermi level, explaining the dramatic evolution of gate-voltage dependent AHE. Combined, the experimental work and calculations shed light on the underlying mechanisms and prospects for electrically tuned vdW spintronic devices.

As a newly synthesized room-temperature vdW magnet, $Cr_{1.2}Te_2$ is noteworthy due to its high remanence near 290 K and the perpendicular magnetic anisotropy up to 300 K [29]. In this study, several $Cr_{1.2}Te_2$ devices were fabricated and subjected to measurements. These are labeled as device No. 1, device No. 2, etc. Figure 1(a) shows the lattice structure of $Cr_{1.2}Te_2$ which has a space group of $P\bar{3}m1$ and exhibits the same intralayer structure (CrTe layer) as $CrTe_2$, while its covalently bonded octahedral vacancies in the vdW gaps are fractionally occupied by the Cr atoms [Cr-2 in Fig. 1(a)]. As the vacancy occupancy rate is ~20% in $Cr_{1.2}Te_2$, the average covalent bond between the adjacent CrTe layers is weaker than the intralayer bonds. This facilitates the mechanical exfoliation of the $Cr_{1.2}Te_2$ nanoflakes. Comprehensive characterization revealed that the Cr/Te ratio is homogeneous throughout the crystals and nanoflakes (see Fig. S1 [32]). Figure 1(b) shows an optical image of a $Cr_{1.2}Te_2$ nanodevice (device No. 1). The atomic force microscopy

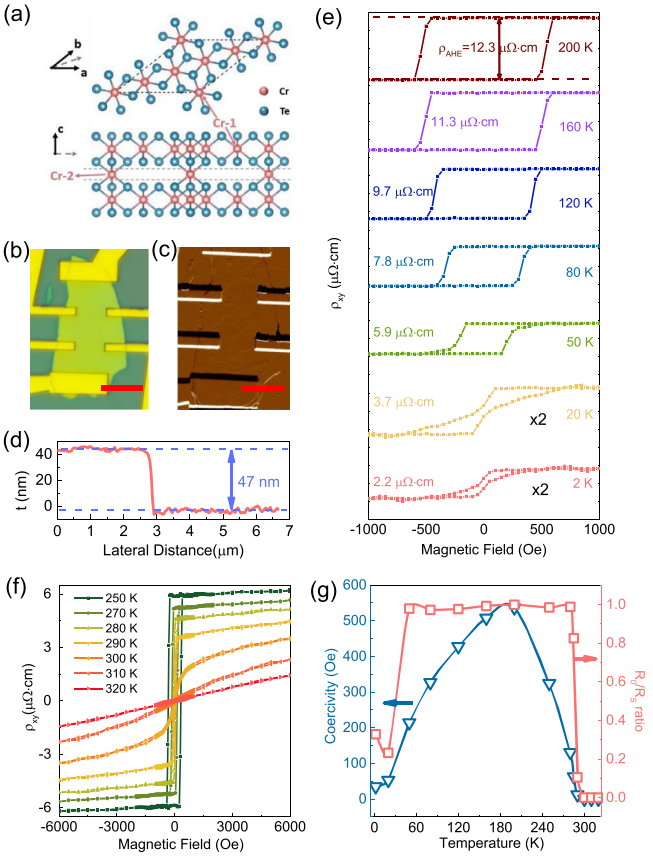

FIG. 1. Crystal structure and initial characterization of device No. 1. (a) Top view and side view of the atomic structure of $Cr_{1.2}Te_2$. The gray dashed line is the bisector of the *a*-*b* axes. Here, Cr-1 is the intralayer Cr atom and Cr-2 represents the interlayer fractional-intercalated Cr atoms. (b),(c) Optical and atomic force microscope images of a $Cr_{1.2}Te_2$ nanoflake (device No. 1) device on a SiO_2/Si substrate. The red scale bars represent 5 μm. (d),(e) AHE hysteresis loops from 2 to 200 K. The scales of ρ_{xy} at 2 and 20 K are zoomed in by 2. (f) AHE curves from 250 to 320 K, the hysteresis disappeared at 300 K. (g) Temperature dependent coercivity and R_0/R_S values.

[Figs. 1(c) and 1(d)] indicates a thickness of around 47 nm. Figure 1(e) shows the AHE curves from 2 to 200 K when the magnetic field is perpendicular to the surface of device No. 1. The ρ_{AHE} values (defined as $2 \times |\rho_{xy}(B = 0.1\ T)|$) of each curve are indicated. At 2 and 20 K, the hysteresis loops deviate from square shaped. From the previous study [29], the as-grown $Cr_{1.2}Te_2$ crystal exhibits in-plane magnetic anisotropy at lower temperatures, while its magnetization easy axis can be rotated from the in-plane to out-of-plane direction when the temperature exceeds 140 K. Here, akin to previous results, near-square shaped hysteresis loops are indicative of perpendicular magnetic anisotropy when the temperature is over 50 K. Figure 1(f) shows the temperature dependent AHE curves recorded above 250 K. These curves became absent at around 320 K, confirming the high Curie temperature of

$Cr_{1.2}Te_2$. The temperature dependent coercivity and remanence curves from 2 to 300 K are displayed in Fig. 1(g). Here, the coercivity is the value of the magnetic field at $\rho_{xy} = 0$ and the remanence is the ratio of $\rho_{xy}(B = 0\ \text{T}, \text{decreased from}\ 2\ \text{T})/\rho_{xy}(B = 0.1\ \text{T})$ (i.e., R_0/R_S ratio). Owing to the in-plane magnetic anisotropy, near-zero coercivities and very small remanences were observed at 2 and 20 K. When the temperature exceeded 50 K, the coercivity first increased with increasing temperature before reaching a peak of 550 Oe at around 200 K. Thereafter, the coercivity decreased with increasing temperature before vanishing when T exceeded 300 K. From 50 to 280 K, the remanence maintained a value of around 1, implying a dominant perpendicular magnetic anisotropy. From 280 K, the remanence started to decrease and finally reached 0 at 300 K, indicating that thermal agitation was then dominant. In this study, we primarily focus on nanoflakes with a thickness of approximately 40 nm. Compared to other thicknesses (see Fig. S3 [32]), their AHE loops maintained a more square shape at higher temperatures.

As stated prior, effective control of the magnetism by a gate voltage represents a significant step in broadening the range of applications for spintronics. Here, using a protonic gate technique, we demonstrate that the ferromagnetism in $Cr_{1.2}Te_2$ nanoflakes can be electrically modulated at temperatures up to and including room temperature. As shown in Fig. 1, the ρ_{AHE}, coercivity and R_0/R_S ratio of device No. 1 reached a peak around 200 K, hence we first investigated the gate tuned AHE loops at 200 K. Figure 2(a) shows a schematic of a solid protonic gate device, in which a voltage is applied between the Pt gate electrode (under the solid protonic electrolyte) and the $Cr_{1.2}Te_2$ nanoflake to drive protons into the nanoflake. Figure 2(a) shows the evolution of the ρ_{xy} loops of a 43 nm thick $Cr_{1.2}Te_2$ nanoflake (device No. 8) under various gate voltages (V_g). When the V_g was increased from 0 to -10 V, the ρ_{AHE} of the near square-shaped loop was increased by a factor approaching three. When the V_g was below -10 V, the ρ_{AHE} dropped sharply and at $V_g = -14$ V, the hysteresis loop became absent. The gate-voltage dependent charge density and R_0/R_S ratio are shown in Fig. 2(a). The hole density decreased by 3.4×10^{21} cm^{-3} (see Fig. S13 [32] for the definition of carrier density) with the increasing proton intercalation resulting from the gate voltage being swept from 0 to -14 V. Hence, significant electron doping is induced by the protonic intercalation. The R_0/R_S ratio remained near 1 under different gate voltages. To clarify the evolution of all the AHE loops, the charge density (n_s) dependent ρ_{AHE} and coercivity are plotted in Fig. 2(a). With increasing proton intercalation, the ρ_{AHE} at first increases slightly, is maintained until $n_s = 2.28 \times 10^{21}$ cm^{-3} ($V_g = -6$ V), then increases again sharply before once again stabilizing from 2.16×10^{21} to 0.98×10^{21} cm^{-3} (V_g from -8 to -10 V). Finally, ρ_{AHE} drops from 13.6 $\mu\Omega \cdot$ cm

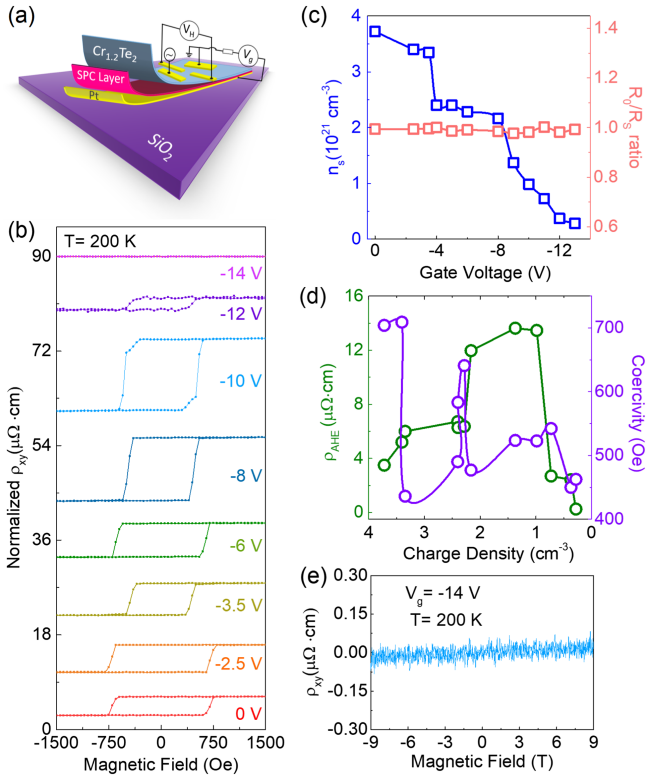

FIG. 2. Protonic gating modulation of a 43 nm $Cr_{1.2}Te_2$ nanoflake (device No. 8) at 200 K. (a) The schematic diagram of a $Cr_{1.2}Te_2$ solid proton conductor (SPC) device, where a $Cr_{1.2}Te_2$ flake lies on the solid proton conductor and a Pt electrode is utilized as the backgate electrode. (b) AHE hysteresis loops under various gate voltages. Here only representative loops are plotted to show the major evolution. (c) Gate voltage dependent charge density and remanence. (d) Evolution of ρ_{AHE} and coercivity values with various charge densities. (e) The Hall effect curve of device No. 8 when $V_g = -14$ V, $T = 200$ K with a magnetic field scan up to 9 T.

to near zero when the voltage increases to -13 V (2.8×10^{20} cm^{-3}). The coercivity declines sharply from 709 to 436 Oe as the hole density decreases from 3.4×10^{21} to 3.34×10^{21} cm^{-3} before rising to a sharp peak of 641 Oe at $n_s = 2.28 \times 10^{21}$ cm^{-3} and undergoing a slight increase from 2.16×10^{21} to 0.72×10^{21} cm^{-3}. The coercivity finally vanishes when V_g is swept to -14 V. The complex evolution of coercivity could indicate that the proton intercalation induced metastable magnetic domain structures within the $Cr_{1.2}Te_2$ nanoflake. Note that the coercivity of a vdW magnetic nanoflake is not solely determined by its thickness, but largely by its evolution of magnetic microstructure, which could be further affected by the defects and impurities generated during the mechanical exfoliation, the size of the nanoflake, the competition between the magnetic anisotropic energy and thermal agitation energy, surface stress, crystal dislocation, intralayer, and interlayer domain wall motions, etc. Hence, it is common to observe several hundred Oersted coercivity bias

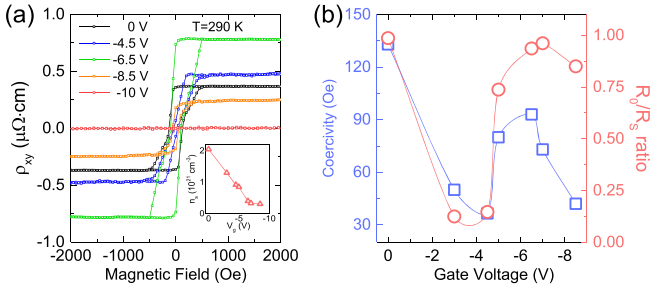

FIG. 3. Voltage-controlled magnetism at 290 K in device No. 4 (43 nm thick). (a) Room temperature AHE loops under different gate voltages. Inset shows the gate voltage dependent charge density. (b) Gate voltage dependent coercivity and R_0/R_S ratio.

between nanoflakes of similar thickness. More gate-voltage dependent AHE loops of device No. 8 and other devices are shown in the Supplemental Material [32]. The absence of hysteresis at $V_g = -14$ V may be attributed to either a MPT or a change in the magnetic anisotropy. If due to the change in magnetic anisotropy from perpendicular to in-plane, a curved hysteresis characteristic would be observed under a large enough applied magnetic field. As shown in Fig. 2(e), with an applied perpendicular field up to 9 T, the AHE curves at $V_g = -14$ V of device No. 8 are nearly flat (Supplemental Material [32] show similarly near-flat Hall curves under 9 T from other devices). This observation effectively rules out the possibility of altered magnetic anisotropy and substantiates the attribution of a protonic gate induced MPT in $Cr_{1.2}Te_2$.

Since the $Cr_{1.2}Te_2$ nanoflakes exhibit a high Curie temperature (up to 320 K) and a nearly square AHE loops up to $T = 290$ K, the gate voltage-controlled magnetism of $Cr_{1.2}Te_2$ nanoflakes was investigated further at 290 K. Figure 3(a) shows the protonic gate-voltage dependent AHE curves of device No. 4 at 290 K. Resembling the results of device No. 8 in Fig. 2, the ρ_{AHE} first increased and reached up to 7.2 $\mu\Omega \cdot$ cm at $V_g = -6.5$ V, a value 4.5 times higher than that of the pristine material (1.6 $\mu\Omega \cdot$ cm). It then sharply declined, and the hysteresis loop vanished at $V_g = -10$ V. The figure inset shows the gate voltage dependent hole density, which decreases with increasing proton intercalation, as in device No. 8. Figure 3(b) shows the gate-voltage dependent coercivity and R_0/R_S ratio at 290 K. As in device No. 8, the coercivity initially falls to 36.5 Oe, (27% of the coercivity at $V_g = 0$ V), then reaches a subpeak at $V_g = -6.5$ V before decreasing to 42 Oe at $V_g = -8.5$ V. The evolution of the R_0/R_S ratio shows a similar trend to the evolution of coercivity which drops to around 0.1 at $V_g = -3$ and -4.5 V and remains around 1 under other gate voltages. Additional AHE data recorded at room temperature from another device (device No. 5) is shown in the Supplemental Material [32]. Based on the aforementioned experimental results, we conclude that electrically tuned MPTs can be realized up to room temperature in proton-gated $Cr_{1.2}Te_2$ devices.

The complex evolution of AHE in $Cr_{1.2}Te_2$ should result from the evolution of magnetic properties and AHC with proton intercalation. To further explore this aspect of the study, theoretical analysis was carried out using density functional theory (DFT). The computational details are included in Supplemental Material [32] (see also Refs. [33–37] therein). Recently, contradictory reports stated that monolayer $CrTe_2$ exhibited a ferromagnetic ground state [24,38], or an antiferromagnetic ground state [39], probably due to different experimental settings and conditions. Our DFT calculations show that the ground state of monolayer $CrTe_2$ is an intralayer antiferromagnetic state in a zigzag pattern, which can be modeled in a rectangular supercell [see Fig. S20(a) [32]]. As the charge density changed by more than 10^{21} cm^{-3} and cross-sectional tunnelling electron microscopy results revealed no significant structural changes with proton intercalation in $Cr_{1.2}Te_2$ (see Fig. S15 [32]), the charge density variation is considered a potential factor in causing the MPT. Here, three magnetic configurations were considered, i.e., FM, AFM, and ferrimagnetic (FerriM), as shown in Fig. 4(a). The charge doping dependent energy for the three magnetic states are illustrated in Fig. 4(b). From the results, $Cr_{1.2}Te_2$ presents the FM state when its hole doping exceeds 1×10^{22} cm^{-3} and the ground state becomes AFM when it is electron doped. Importantly, when the hole doping decreases within the range $n_s = 10^{22}$ to 0 cm^{-3}, the magnetic ground state changes from FM to AFM. This is qualitatively consistent with the experiments. Meanwhile, introducing protons into $Cr_{1.2}Te_2$, in terms of charge, equivalent to injecting electrons (H^-) into the system [17], pushes the Fermi level significantly higher (see Fig. S17 [32]). Increases of around 0.19 and 1.78 eV result for $Cr_{1.2}Te_2H_{0.2}$ and $Cr_{1.2}Te_2H_2$, respectively, indicating remarkable electronic doping due to the proton intercalation. These results suggest that the proton intercalation-induced electron doping could bias energies of different ground states and thereby contribute to the evolution in the gate-dependent magnetic hysteresis loops. Ultimately, a FM to AFM MPT is induced, as observed in the experiment.

To understand the remanence variation with applied gate voltages shown in Fig. 2 and Fig. 3, the AHC under gate voltages were analyzed. A tight-binding Hamiltonian for $Cr_{1.2}Te_2$ was built via the WANNIER90 package based on the Cr d and Te p orbitals [40–42]. The AHC was calculated based on the method of Berry curvature, employing the WannierTools codes [43,44]. The calculated band structure, AHC, and partial density of states (PDOS), of $Cr_{1.2}Te_2$ are presented in Figs. 4(c)–4(e), respectively. The density of states near the Fermi level is mainly determined by the d orbitals of the Cr atoms and the p orbitals of the Te atoms. Significant σ_{xy} and σ_{yz} AHC components coexist in the

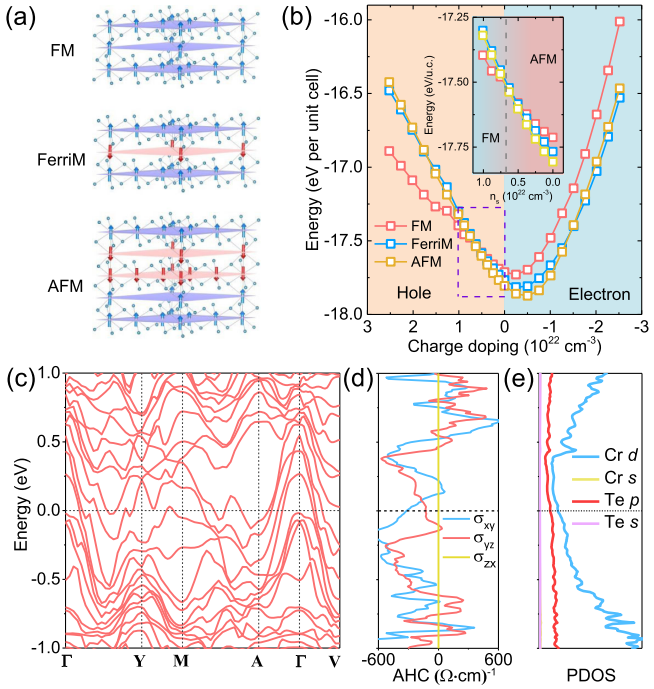

FIG. 4. DFT calculations. (a) Three potential magnetic configurations for $Cr_{1.2}Te_2$. The blue and red arrows represent spin up and down, respectively. (b) Total energy as a function of charge density with three magnetic configurations. Inset is an enlargement of the purple dashed rectangular section corresponding to the experimental range. (c) Band structure, (d) anomalous Hall conductivity, and (e) PDOS of $Cr_{1.2}Te_2$, respectively.

material. This phenomenon results from the in-plane magnetization of the doped Cr atoms and the out-of-plane magnetization of the other Cr atoms. This characteristic differs from that observed in ordinary AHC materials, in which the magnetic moments align almost colinearly along the magnetic easy axis and only one significant AHC component exists [45]. It is obvious that the calculated AHC varies significantly near the Fermi level. As mentioned earlier, the Fermi level is significantly elevated due to proton intercalation. Consequently, the AHC values may be altered. Combining the calculations of AHC in Fig. 4(d) and possible magnetic states in Fig 4(b), we can conclude that the ρ_{AHE} evolution with various gate voltages does not originate from the variation of magnetization but from the large variation of AHC due to appreciable Fermi level shift.

In conclusion, based on experimental results and DFT calculations, we have confirmed an electrically manipulated FM to AFM transition in $Cr_{1.2}Te_2$, a vdW itinerant ferromagnet with a near square-shaped magnetic loop that is maintained up to room temperature. This was achieved using protonic gating, demonstrating the effectiveness of this tool for modulating the magnetic properties of low-dimensional materials. The realization of room-temperature electrically tuned magnetism in vdW magnets with a near square-shaped magnetic loop is a vital step towards the commercial application of vdW magnetic heterostructures-based spintronic devices. With the emergence of AFM spintronics, the observation of an electrically tuned FM-AFM phase transition at room temperature is significant and suggests $Cr_{1.2}Te_2$ nanoflakes as a potential platform for novel AFM spintronic devices.

This research was performed in part at the RMIT Micro Nano Research Facility (MNRF) in the Victorian Node of the Australian National Fabrication Facility (ANFF) and the RMIT Microscopy and Microanalysis Facility (RMMF). L. W. was supported by the Australian Research Council Centre of Excellence in Future Low-Energy Electronics Technologies (Project No. CE170100039), the National Natural Science Foundation of China (Grants No. 12374177, No. 52072102, and No. 12235015) and the Funding for Infrastructure and Facility at Hefei University of Technology. Work at South China University of Technology was supported by the National Natural Science Foundation of China (Grant No. 12074126) and the Key Research and Development Project of Guangdong Province (Grant No. 2020B0303300001). Work at High Magnetic Field Laboratory was supported by National Key R&D Program of the MOST of China (Grant No. 2022YFA1602603), the National Natural Science Foundation of China (Grants No. 12274413, No. U19A2093) and Collaborative Innovation Program of Hefei Science Center, CAS (Grant No. 2022HSC-CIP017). Work at University of Science and Technology of China was supported by the Innovation Program for Quantum Science and Technology (2021ZD0302800).

*These authors equally contributed to the Letter.
†Corresponding author: glzheng@hmfl.ac.cn
‡Corresponding author: binxiang@ustc.edu.cn
§Corresponding author: zhaoyj@scut.edu.cn
‖Corresponding author: wanglan@hfut.edu.cn

[1] H. Ohno, D. Chiba, F. Matsukura, T. Omiya, E. Abe, T. Dietl, Y. Ohno, and K. Ohtani, Electric-field control of ferromagnetism, Nature (London) **408**, 944 (2000).
[2] S. A. Wolf, D. D. Awschalom, R. A. Buhrman, J. M. Daughton, S. von Molnár, M. L. Roukes, A. Y. Chtchelkanova, and D. M. Treger, Spintronics: A spin-based electronics vision for the future, Science **294**, 1488 (2001).
[3] D. Chiba, M. Yamanouchi, F. Matsukura, and H. Ohno, Electrical manipulation of magnetization reversal in a ferromagnetic semiconductor, Science **301**, 943 (2003).
[4] I. Žutić, J. Fabian, and S. Das Sarma, Spintronics: Fundamentals and applications, Rev. Mod. Phys. **76**, 323 (2004).
[5] F. Matsukura, Y. Tokura, and H. Ohno, Control of magnetism by electric fields, Nat. Nanotechnol. **10**, 209 (2015).
[6] C. Gong, L. Li, Z. Li, H. Ji, A. Stern, Y. Xia, T. Cao, W. Bao, C. Wang, Y. Wang *et al.*, Discovery of intrinsic ferromagnetism in two-dimensional van der Waals crystals, Nature (London) **546**, 265 (2017).

[7] B. Huang, G. Clark, E. Navarro-Moratalla, D. R. Klein, R. Cheng, K. L. Seyler, D. Zhong, E. Schmidgall, M. A. McGuire, D. H. Cobden *et al.*, Layer-dependent ferromagnetism in a van der Waals crystal down to the monolayer limit, Nature (London) **546**, 270 (2017).

[8] D. R. Klein, D. MacNeill, J. L. Lado, D. Soriano, E. Navarro-Moratalla, K. Watanabe, T. Taniguchi, S. Manni, P. Canfield, J. Fernández-Rossier *et al.*, Probing magnetism in 2D van der Waals crystalline insulators via electron tunnelling, Science **360**, 1218 (2018).

[9] T. Song, X. Cai, M. W.-Y. Tu, X. Zhang, B. Huang, N. P. Wilson, K. L. Seyler, L. Zhu, T. Taniguchi, K. Watanabe *et al.*, Giant tunneling magnetoresistance in spin-filter van der Waals heterostructures, Science **360**, 1214 (2018).

[10] Z. Wang, D. Sapkota, T. Taniguchi, K. Watanabe, D. Mandrus, and A. F. Morpurgo, Tunneling spin valves based on $Fe_3GeTe_2/hBN/Fe_3GeTe_2$ van der Waals heterostructures, Nano Lett. **18**, 4303 (2018).

[11] S. Albarakati, C. Tan, Z.-J. Chen, J. G. Partridge, G. Zheng, L. Farrar, E. L. H. Mayes, M. R. Field, C. Lee, Y. Wang *et al.*, Antisymmetric magnetoresistance in van der Waals Fe_3GeTe_2/graphite/Fe_3GeTe_2 trilayer heterostructures, Sci. Adv. **5**, eaaw0409 (2019).

[12] S. Jiang, J. Shan, and K. F. Mak, Electric-field switching of two-dimensional van der Waals magnets, Nat. Mater. **17**, 406 (2018).

[13] S. Jiang, L. Li, Z. Wang, K. F. Mak, and J. Shan, Controlling magnetism in 2D CrI_3 by electrostatic doping, Nat. Nanotechnol. **13**, 549 (2018).

[14] I. A. Verzhbitskiy, H. Kurebayashi, H. Cheng, J. Zhou, S. Khan, Y. P. Feng, and G. Eda, Controlling the magnetic anisotropy in $Cr_2Ge_2Te_6$ by electrostatic gating, Nat. Electron. **3**, 460 (2020).

[15] B. Huang, G. Clark, D. R. Klein, D. MacNeill, E. Navarro-Moratalla, K. L. Seyler, N. Wilson, M. A. McGuire, D. H. Cobden, D. Xiao *et al.*, Electrical control of 2D magnetism in bilayer CrI_3, Nat. Nanotechnol. **13**, 544 (2018).

[16] C. Tan, W.-Q. Xie, G. Zheng, N. Aloufi, S. Albarakati, M. Algarni, J. Li, J. Partridge, D. Culcer, X. Wang *et al.*, Gate-controlled magnetic phase transition in a van der Waals magnet Fe_5GeTe_2, Nano Lett. **21**, 5599 (2021).

[17] G. Zheng, W.-Q. Xie, S. Albarakati, M. Algarni, C. Tan, Y. Wang, J. Peng, J. Partridge, L. Farrar, J. Yi *et al.*, Gate-Tuned Interlayer Coupling in van der Waals Ferromagnet Fe_3GeTe_2 Nanoflakes, Phys. Rev. Lett. **125**, 047202 (2020).

[18] S. Albarakati, W.-Q. Xie, C. Tan, G. Zheng, M. Algarni, J. Li, J. Partridge, M. J. S. Spencer, L. Farrar, Y. Xiong *et al.*, Electric control of exchange bias effect in $FePS_3-Fe_5GeTe_2$ van der Waals heterostructures, Nano Lett. **22**, 6166 (2022).

[19] J. Dijkstra, H. H. Weitering, C. F. van Bruggen, C. Haas, and R. A. de Groot, Band-structure calculations, and magnetic and transport properties of ferromagnetic chromium tellurides (CrTe, Cr_3Te_4, Cr_2Te_3), J. Phys. Condens. Matter **1**, 9141 (1989).

[20] Y. Liu and C. Petrovic, Critical behavior of the quasi-two-dimensional weak itinerant ferromagnet trigonal chromium telluride $Cr_{0.62}Te$, Phys. Rev. B **96**, 134410 (2017).

[21] X. Sun, W. Li, X. Wang, Q. Sui, T. Zhang, Z. Wang, L. Liu, D. Li, S. Feng, S. Zhong *et al.*, Room temperature ferromagnetism in ultra-thin van der Waals crystals of 1T-$CrTe_2$, Nano Res. **13**, 3358 (2020).

[22] Y. Wen, Z. Liu, Y. Zhang, C. Xia, B. Zhai, X. Zhang, G. Zhai, C. Shen, P. He, R. Cheng *et al.*, Tunable room-temperature ferromagnetism in two-dimensional Cr_2Te_3, Nano Lett. **20**, 3130 (2020).

[23] L. Meng, Z. Zhou, M. Xu, S. Yang, K. Si, L. Liu, X. Wang, H. Jiang, B. Li, P. Qin *et al.*, Anomalous thickness dependence of Curie temperature in air-stable two-dimensional ferromagnetic 1T-$CrTe_2$ grown by chemical vapor deposition, Nat. Commun. **12**, 809 (2021).

[24] X. Zhang, Q. Lu, W. Liu, W. Niu, J. Sun, J. Cook, M. Vaninger, P. F. Miceli, D. J. Singh, S.-W. Lian *et al.*, Room-temperature intrinsic ferromagnetism in epitaxial $CrTe_2$ ultrathin films, Nat. Commun. **12**, 2492 (2021).

[25] M. Huang, S. Wang, Z. Wang, P. Liu, J. Xiang, C. Feng, X. Wang, Z. Zhang, Z. Wen, H. Xu *et al.*, Colossal anomalous Hall effect in ferromagnetic van der Waals $CrTe_2$, ACS Nano **15**, 9759 (2021).

[26] B. Li, Z. Wan, C. Wang, P. Chen, B. Huang, X. Cheng, Q. Qian, J. Li, Z. Zhang, G. Sun *et al.*, Van der Waals epitaxial growth of air-stable $CrSe_2$ nanosheets with thickness-tunable magnetic order, Nat. Mater. **20**, 818 (2021).

[27] B. Tang, X. Wang, M. Han, X. Xu, Z. Zhang, C. Zhu, X. Cao, Y. Yang, Q. Fu, J. Yang *et al.*, Phase engineering of Cr_5Te_8 with colossal anomalous Hall effect, Nat. Electron. **5**, 224 (2022).

[28] H. Zheng, C. Huang, F. Lin, J. Fan, H. Liu, L. Zhang, C. Ma, C. Wang, Y. Zhu, and H. Yang, Two-dimensional van der Waals ferromagnetic thin film $CrTe_2$ with high Curie temperature and metallic conductivity, Appl. Phys. Lett. **122**, 023103 (2023).

[29] M. Huang, L. Gao, Y. Zhang, Y. Zhang, X. Lei, G. Hu, J. Xiang, H. Zeng, X. Fu, Z. Zhang *et al.*, Possible topological Hall effect above room temperature in layered $Cr_{1.2}Te_2$ ferromagnet, Nano Lett. **21**, 4280 (2021).

[30] Y. Deng, Y. Yu, Y. Song, J. Zhang, N. Z. Wang, Z. Sun, Y. Yi, Y. Z. Wu, S. Wu, J. Zhu *et al.*, Gate-tunable room-temperature ferromagnetism in two-dimensional Fe_3GeTe_2, Nature (London) **563**, 94 (2018).

[31] G. Zheng, M. Wang, X. Zhu, C. Tan, J. Wang, S. Albarakati, N. Aloufi, M. Algarni, L. Farrar, M. Wu *et al.*, Tailoring Dzyaloshinskii-Moriya interaction in a transition metal dichalcogenide by dual-intercalation, Nat. Commun. **12**, 3639 (2021).

[32] See Supplemental Material at http://link.aps.org/supplemental/10.1103/PhysRevLett.131.166703 for methods of experiment and theory, which includes Refs. [33–37].

[33] P. Zomer, M. Guimarães, J. Brant, N. Tombros, and B. J. Van Wees, Fast pick up technique for high quality heterostructures of bilayer graphene and hexagonal boron nitride, Appl. Phys. Lett. **105**, 013101 (2014).

[34] G. Kresse and J. Furthmüller, Efficient iterative schemes for *ab initio* total-energy calculations using a plane-wave basis set, Phys. Rev. B **54**, 11169 (1996).

[35] H. J. Monkhorst and J. D. Pack, Special points for Brillouin-zone integrations, Phys. Rev. B **13**, 5188 (1976).

[36] S. Grimme, J. Antony, S. Ehrlich, and H. Krieg, A consistent and accurate *ab initio* parametrization of density functional dispersion correction (DFT-D) for the 94 elements H-P, J. Chem. Phys. **132**, 154104 (2010).

[37] J. P. Perdew, K. Burke, and M. Ernzerhof, Generalized Gradient Approximation Made Simple, Phys. Rev. Lett. **77**, 3865 (1996).

[38] Y. Ou, W. Yanez, R. Xiao, M. Stanley, S. Ghosh, B. Zheng, W. Jiang, Y.-S. Huang, T. Pillsbury, A. Richardella *et al.*, $ZrTe_2/CrTe_2$: An epitaxial van der Waals platform for spintronics, Nat. Commun. **13**, 2972 (2022).

[39] J.-J. Xian, C. Wang, J.-H. Nie, R. Li, M. Han, J. Lin, W.-H. Zhang, Z.-Y. Liu, Z.-M. Zhang, M.-P. Miao *et al.*, Spin mapping of intralayer antiferromagnetism and field-induced spin reorientation in monolayer $CrTe_2$, Nat. Commun. **13**, 257 (2022).

[40] N. Marzari and D. Vanderbilt, Maximally localized generalized Wannier functions for composite energy bands, Phys. Rev. B **56**, 12847 (1997).

[41] I. Souza, N. Marzari, and D. Vanderbilt, Maximally localized Wannier functions for entangled energy bands, Phys. Rev. B **65**, 035109 (2001).

[42] A. A. Mostofi, J. R. Yates, Y.-S. Lee, I. Souza, D. Vanderbilt, and N. Marzari, WANNIER90: A tool for obtaining maximally-localised Wannier functions, Comput. Phys. Commun. **178**, 685 (2008).

[43] Y. G. Yao, L. Kleinman, A. H. MacDonald, J. Sinova, T. Jungwirth, D. S. Wang, E. G. Wang, and Q. Niu, First Principles Calculation of Anomalous Hall Conductivity in Ferromagnetic bcc Fe, Phys. Rev. Lett. **92**, 037204 (2004).

[44] Q. Wu, S. Zhang, H.-F. Song, M. Troyer, and A. A. Soluyanov, WannierTools: An open-source software package for novel topological materials, Comput. Phys. Commun. **224**, 405 (2018).

[45] J.-Y. Lin, Z.-J. Chen, W.-Q. Xie, X.-B. Yang, and Y.-J. Zhao, Toward ferromagnetic semimetal ground state with multiple Weyl nodes in van der Waals crystal $MnSb_4Te_7$, New J. Phys. **24**, 043033 (2022).